

Drift and breakup of spiral waves in reaction–diffusion–mechanics systems

A. V. Panfilov*[†], R. H. Keldermann*, and M. P. Nash*

*Department of Theoretical Biology, Utrecht University, Padualaan 8, Utrecht 3584 CH, The Netherlands; and [†]Bioengineering Institute and Department of Engineering Science, University of Auckland, Auckland, New Zealand

Communicated by Charles S. Peskin, New York University, New York, NY, March 3, 2007 (received for review January 24, 2006)

Rotating spiral waves organize excitation in various biological, physical, and chemical systems. They underpin a variety of important phenomena, such as cardiac arrhythmias, morphogenesis processes, and spatial patterns in chemical reactions. Important insights into spiral wave dynamics have been obtained from theoretical studies of the reaction–diffusion (RD) partial differential equations. However, most of these studies have ignored the fact that spiral wave rotation is often accompanied by substantial deformations of the medium. Here, we show that joint consideration of the RD equations with the equations of continuum mechanics for tissue deformations (RD–mechanics systems), yield important effects on spiral wave dynamics. We show that deformation can induce the breakup of spiral waves into complex spatiotemporal patterns. We also show that mechanics leads to spiral wave drift throughout the medium approaching dynamical attractors, which are determined by the parameters of the model and the size of the medium. We study mechanisms of these effects and discuss their applicability to the theory of cardiac arrhythmias. Overall, we demonstrate the importance of RD–mechanics systems for mathematics applied to life sciences.

electromechanics | nonlinear dynamics | stretch-activated channels | cardiac arrhythmias

Rotating spiral waves have been found in a wide variety of nonlinear systems in physics, chemistry, and biology. For example, they occur in Belousov–Zhabotinsky (BZ) chemical reactions (1, 2) and on platinum surfaces during the process of catalytic oxidation of carbon monoxide (3). Biological examples of spiral waves include spiral waves during morphogenesis of the *Dictyostelium discoideum* amoebae (4), spiral waves of calcium-induced calcium release in *Xenopus* oocytes (5), and spiral waves in retinal and cortical nerve tissue (2). Another important example is in the heart, for which spiral waves of electrical activity are thought to lead to life-threatening cardiac arrhythmias (2, 6).

Spiral waves have been studied extensively by using mathematical modeling. In this context, spiral waves are solutions of the reaction–diffusion (RD) equations in two dimensions. There are a wide range of analytical and numerical approaches to study the basic features of these systems, as well as specific models for a variety of biological or chemical processes.

Spiral wave rotation typically is accompanied by other important processes. One of the most fundamental is the mechanical deformation of the medium. For example, spiral waves during *D. discoideum* morphogenesis are relayed by chemotactically moving cells (4), and chemical spiral waves in BZ reaction cause deformation of the medium in which they rotate (7). In the heart, the electrical waves initiate muscle contraction, resulting in substantial local deformations. These deformations in turn affect the process of wave propagation in the heart, which is known as the phenomenon of mechano-electrical feedback. Mechano-electrical feedback has been studied in electrophysiology for over a century (see reviews in ref. 8) and may have both anti- and pro-arrhythmic consequences. Although deformation is known to be important in the above-mentioned systems, most previous theoretical and ex-

perimental studies have not addressed the combined effects of medium mechanics and spiral wave dynamics.

To study the interactive effects of deformation and RD systems, one needs to combine two classes of partial differential equations: the RD equations (as above) and the equations of continuum mechanics, which govern the deformation of the medium. Furthermore, one must define the feedback relations that exist between them. In the heart, local deformations of up to 10–15% have been observed experimentally (9), thus finite deformation elasticity theory must be used to describe the tissue mechanics. The detailed coupling of the RD processes and mechanical deformations is complex and not completely understood; however, general relationships have been established. For example, it is well known that heart tissue contraction is initiated by an influx of calcium ions into the cardiac myocytes, which is a typical state variable of biophysical RD models (10). On the other hand, deformation changes the geometry of cardiac cells and ionic currents through the cardiac membrane [via stretch-activated channels (11)], thereby affecting the parameters of the RD system. We have proposed the concept of a RD–mechanics (RDM) system (12), which combines a very general description of deformation with a low-dimensional RD system to study the basic effects of mechanics on nonlinear wave propagation.

In this article, we apply our RDM modeling approach to study the fundamental effects of deformation on spiral wave dynamics. We find two types of dynamics: mechanically induced breakup of spiral waves and drift of spiral waves toward dynamical attractors caused by mechanical deformation. These types of dynamics may be important in many applications. For example, in cardiac tissue, spiral breakup is considered as a likely mechanism of ventricular fibrillation, whereas meander and drift of spiral waves are believed to determine the type of cardiac arrhythmia (13, 14).

Mathematical Model

Our RDM model is based on a three-variable Fenton–Karma RD model for cardiac excitation (15), coupled with the soft-tissue mechanics equations described in refs. 12 and 16:

$$\frac{\partial u}{\partial t} = \nabla^2 u - I_{fi}(u, v) - I_{so}(u) - I_{si}(u, w) - I_s(u, C), \quad [1]$$

$$\frac{\partial v}{\partial t} = \frac{\Theta(u_c - u) - v}{\tau_v(u)}, \quad [2]$$

Author contributions: A.V.P. and M.P.N. designed research; A.V.P. and R.H.K. performed research; and A.V.P., R.H.K., and M.P.N. wrote the paper.

The authors declare no conflict of interest.

Abbreviations: RD, reaction–diffusion; RDM, RD–mechanics; BZ, Belousov–Zhabotinsky; [t.u.], dimensionless time units; [s.u.], dimensionless space units.

[†]To whom correspondence should be addressed. E-mail: a.panfilov@uu.nl.

This article contains supporting information online at www.pnas.org/cgi/content/full/0701895104/DC1.

© 2007 by The National Academy of Sciences of the USA

$$\frac{\partial w}{\partial t} = \frac{\Theta(u - 0.25) - w}{\tau_w(u)}, \quad [3]$$

$$\frac{\partial T_a}{\partial t} = \varepsilon(u)(k_T u - T_a), \quad [4]$$

$$\frac{\partial}{\partial X_M} \left(T^{MN} \frac{\partial x_j}{\partial X_N} \right) = 0, \quad [5]$$

$$T^{MN} = \frac{1}{2} \left(\frac{\partial W}{\partial E_{MN}} + \frac{\partial W}{\partial E_{NM}} \right) + T_a C_{MN}^{-1}, \quad [6]$$

$$\nabla^2 u = \frac{\partial}{\partial X_M} \left(\sqrt{C} C_{MN}^{-1} \frac{\partial u}{\partial X_N} \right), \quad [7]$$

where $\Theta(x)$ is the standard Heaviside step function: $\Theta(x) = 1$ for $x \geq 0$ and $\Theta(x) = 0$ for $x < 0$. Eqs. 1–3 provide a standard low-dimensional model of cardiac electrical propagation, which includes a qualitative description of three main ionic currents that modulate the activation of cardiac tissue: the fast inward current $I_{fi}(u, v) = -g_{fi}v\Theta(u - 0.25)(1 - u)(u - 0.25)$, with a maximal conductance of $g_{fi} = 7.2$, determines the primary excitation of a cell; the slow outward current $I_{so}(u) = 0.05u^{1.4}\Theta(0.2 - u)$ accounts for recovery of cell properties after excitation; the slow inward current $I_{si}(u, w) = \Theta(u - 0.2)uw(0.46 + 0.085 \cdot \tanh[k(u - 0.5)])$ determines the duration of the excitation pulse; and $I_s(u, c) =$ the stretch-activated current, which will be described later. The variable u represents the (nondimensional) transmembrane potential scaled to the interval $[0, 1]$.

The Hodgkin–Huxley-type gating variable v determines inactivation of I_{fi} , with the time constant given by: $\tau_v(u) = \tau_1$ for $u \leq 0.085$; $\tau_v(u) = \tau_2$ for $0.085 < u < 0.125$; $\tau_v(u) = \tau_3$ for $0.125 \leq u < u_c$; and $\tau_v(u) = \tau_4$ for $u \geq u_c$. The gating variable w determines activation of I_{si} , with the time constant $\tau_w(u) = 125$ for $u \leq 0.25$ and $\tau_w(u) = 170$ for $u > 0.25$. The currents I_{fi} , I_{so} , and I_{si} may be regarded as general descriptions of the sodium, potassium, and calcium currents, respectively, of an excitable cardiac cell.

After excitation, the tissue in our model contracts, and the mechanics are modulated by the variable T_a (given by Eq. 4), which represents the active stress generated by the medium. The function $\varepsilon(u) = 1$ for $u \leq 0.05$ and $\varepsilon(u) = 0.1$ for $u > 0.05$ governs the delay between activation and active force development. k_T governs the rate of tension development during excitation and thus the maximal value of active tension. Doubling k_T results in an approximate two-fold increase in active tension.

The mechanical part of our model is unchanged from ref. 16. The main equations here are the equations of stress equilibrium (Eq. 5) formulated by using the second Piola–Kirchhoff stress tensor, T^{MN} in Eq. 6, which contains two parts: (i) the active stress components, $T_a C_{MN}^{-1}$, where $C_{MN} = \partial x_k / \partial X_M \cdot \partial x_k / \partial X_N$ is the right Cauchy–Green deformation (metric) tensor and C is its determinant and (ii) the passive elastic stress components, which are expressed in terms of the derivatives of a strain energy function (W) with respect to components of Green’s strain tensor, $E_{MN} = 1/2(C_{MN} - \delta_{MN})$, where δ_{MN} is the unitary tensor. For the purposes of this study, the strain energy function was chosen to be the isotropic Mooney–Rivlin constitutive law (17), $W = c_1(I_1 - 3) + c_2(I_2 - 3)$, where I_1 and I_2 are principal invariants of C_{MN} and c_1 and c_2 are stiffness coefficients that, together with the parameter k_T from Eq. 4, determine local deformation during contraction ($c_1 = 2$, $c_2 = 6$, and $k_T = 10$ for all simulations, chosen to give rise to relative local deformations of $\approx 15\%$).

The direct influence of deformation on the excitation properties is given by the stretch-activated current I_s . In general, there

are three groups of mechanically activated channels in the heart, but only two of them (the cation nonselective channels and the potassium-selective channels) are activated by stretch (11). The overall physiological action of these channels is depolarization of the membrane in response to stretch, as shown in the majority of experimental observations from isolated cardiac tissue and the whole heart. Experimental studies of the electrophysiological properties of stretch-activated channels show that they are activated instantly by mechanical stimulation, and the current–voltage (I – V) relationship for the most important nonspecific cation channel is linear (18, 19). On the basis of these observations, linear ionic models for I_s have been proposed (20, 21). These linear models have been used to study the effects of mechanical stretch on heart tissue by using detailed ionic models of the cardiac myocyte. Therefore, we believe that a linear time-independent description also will be sufficient for our low-dimensional formulation for cardiac cells. Thus, we use

$$I_s = G_s(\sqrt{C} - 1)(u - E_s), \quad [8]$$

where G_s and E_s are the maximal conductance and reversal potential, respectively, of the stretch-activated channels. Following ref. 16, the current in Eq. 8 is present only if $\sqrt{C} > 1$ (which indicates stretch).

The value of E_s in most biophysically accurate models is assumed to be around -20 mV (18, 20) and describes the experimentally observed depolarizing effect of the stretch-activated current. In our model, we used values close to $E_s \sim 1$ to provide the depolarizing effect. However, the exact value of the reversal potential may depend on the cell type (11, 18, 19); therefore, we performed simulations with lower values of E_s to investigate the possible effects on the main results of this study.

The value of G_s is one of the main determinants of the effects of deformation on wave propagation and was varied in our computations. The complete list of parameters of the models used in this study is given in [supporting information \(SI\) Table 1](#).

Numerical Integration Methods. The coupled RDM model was solved by using a hybrid approach that combines an explicit Euler scheme for the RD system, with nonlinear finite element techniques for large deformation mechanics. Full details are given in refs. 12 and 16. The numerical parameters were the following. Euler computations were performed on a deforming grid of up to 513×513 finite difference points by using no-flux boundary conditions. For all simulations, we used a time integration step of $\Delta t = 0.1$ (dimensionless time units [t.u.]) and a space integration step of $\Delta x = \Delta y = 0.8$ (dimensionless space units [s.u.]), consistent with previous studies involving a similar RD model (15). Each mechanical element contained between 6×6 and 33×33 electrical grid points, and the mechanics solution steps were separated by between 10 and 80 excitation integration steps (consistent with refs. 12 and 16). When solving Eq. 5, the boundaries of the medium were fixed in space, which is consistent with an isometric contraction regime, a standard experimental procedure for muscle mechanics, during which end points or edges of the tissue are fixed to maintain a constant overall dimension. Isometric contraction is appropriate for isovolumic phases of contraction and relaxation during the cardiac cycle, for which the overall dimension of the heart is approximately constant, whereas regional deformations are heterogeneously distributed.

Results

Spiral Wave Breakup. In the absence of deformation, Eqs. 1–3 describes nonoscillatory cardiac tissue that supports stable rotating spiral waves (Fig. 1a). We found that in the presence of deformation (Eqs. 1–8), rotation of spiral waves became unstable and broke up

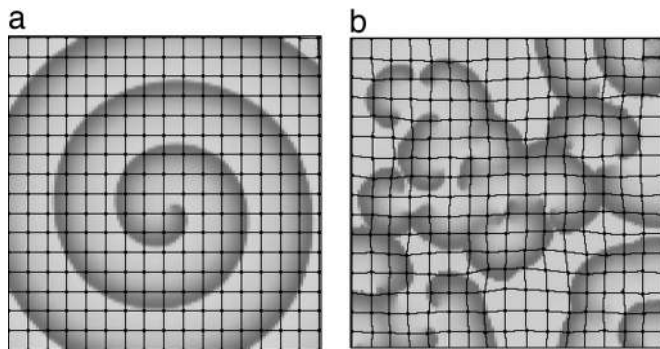


Fig. 1. Spiral wave breakup caused by mechanical activity. (a) Spiral wave rotation in a RD system based on Eqs. 1–3 and in the absence of deformation with $u_c = 0.15$, $\tau_1 = \tau_2 = \tau_3 = 30$, and $\tau_4 = 3$. (b) Similar computations in a deforming medium using Eqs. 1–8 with $G_s = 0.03$. Both snapshots are taken at 1,800 [t.u.]. The medium consists of 513×513 grid points and 16×16 mechanical elements, each containing 33×33 grid points.

into complex spatiotemporal patterns (Fig. 1b) that persisted for the duration of our simulations (≈ 50 rotations).

We investigated the factors underpinning the transition from a stable rotating spiral into spiral breakup. In Eqs. 1–3, the main influence of mechanical deformation on excitation appears in two ways: (i) via the stretch-activated current I_s in Eq. 1 and (ii) caused by deformation of the tissue, as expressed in Eq. 7. We studied the relative contributions of these two factors to the spiral wave instability. We performed one simulation using the same parameter values and initial conditions as the simulation in Fig. 1b but in the absence of I_s . In this case, spiral wave stability persisted despite the tissue deformations (SI Fig. 6a).

In another simulation, I_s was maintained similarly to the computation illustrated in Fig. 1b, but the effect of tissue deformation on wave propagation was neglected [i.e., rather than by using Eq. 7, the Laplacian was evaluated by using $\nabla^2 u = (\partial^2/\partial X^2) + (\partial^2/\partial Y^2)$, as for the undeformed configuration]. In this case, we observed that the onset of spiral breakup, and its subsequent complexity, was similar to the simulation in Fig. 1b (see SI Fig. 6b).

In additional sets of computations, we found that spiral breakup occurred only if the conductance of the stretch-activated channel was $G_s \geq 0.028$. We found that this threshold value (which we denote as G_{sTH}) was modulated by other parameters of the model that influence the stretch-activated current in Eq. 8. If the reversal potential for the stretch-activated current was decreased to $E_s = 0.75$, then the conductance threshold for breakup increased to $G_{sTH} = 0.039$, and a further decrease to $E_s = 0.5$ resulted in $G_{sTH} = 0.065$. Clearly, decreasing E_s in Eq. 8 reduces the magnitude of the stretch-activated current, and thus a larger value of G_s is necessary for breakup to occur. The complete dependence of G_{sTH} on E_s is illustrated in SI Fig. 7.

The observation that mechanically induced spiral wave breakup was primarily caused by the stretch-activated current was somewhat unexpected, because it is a depolarizing current, and such currents typically promote excitation in cardiac tissue. Thus, we investigated how propagation block could be caused by the stretch-activated current, and it turns out that the mechanism of this effect is related to the so-called “accommodation phenomenon,” whereby the threshold for activation increases as the rate of depolarization is decreased. This effect has been studied in electrophysiology since 1936 (22, 23).

We illustrate this effect by using an example that incorporates a recent detailed ionic model for human cardiac cells (24). This model uses a widely accepted biophysical description of the

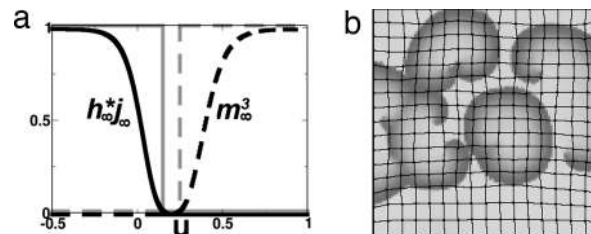


Fig. 2. Breakup in a model with biophysical activation and inactivation of the fast inward current I_{fi} . (a) The scaled activation and inactivation curves from the TNNP model (24) (black lines). (The values are scaled from the original values of voltage to the interval of voltage between 0 and 1 for the Fenton–Karma model.) Plotted are the scaled curves of $h_\infty(u) \times j_\infty(u)$ (solid black line) and of $m_\infty^3(u)$ (dashed black line) from ref. 24. The gray lines show the Heaviside description of the activation (dashed gray line) and inactivation (solid gray line) curves in Eqs. 1–3. (b) Spiral wave breakup in a model with biophysical activation and inactivation of the fast inward current I_{fi} (see text for details). The snapshot is taken at 1,200 [t.u.], $g_{fi} = 14.2$, and all other parameters and initial conditions are the same as in Fig. 1.

sodium current, for which conductance of the sodium channels is proportional to the product of activation (m) and inactivation (h, j) gates: $I_{Na} \sim m^3 h j$. Following the Hodgkin–Huxley approach (23), the dynamics of the gating variables are given by equations of the form: $dm/dt = (m_\infty(u) - m)/\tau_m(u)$, where the parameters of the voltage-dependent functions $m_\infty(u)$ and $\tau_m(u)$ are fitted to experimental measurements. Similar exponential relaxation equations are used for the h and j gates. The steady-state values $m_\infty(u)$, $h_\infty(u)$, and $j_\infty(u)$ depend on the transmembrane voltage and are shown in Fig. 2a. As voltage increases, we see that the activation gate goes from 0 to 1, and the inactivation gate goes from 1 to 0. It is important to note that the inactivation curve approaches zero at a voltage of around $u \sim 0.15$, whereas the activation curve starts to increase for higher values of voltage above about $u \sim 0.25$. Thus, if cardiac tissue is depolarized slowly from the resting state $u = 0$ such that the gating variables approximately follow their steady-state values, then I_{Na} will be inactivated (at $u = 0.15$) before the voltage reaches the activation threshold ($u = 0.25$). A similar situation will occur if cardiac tissue is incompletely repolarized after excitation such that the resting potential is above the inactivation value of $u = 0.15$. This type of I_{Na} inactivation occurs in our simulations and results in spiral wave breakup.

This finding is illustrated in Fig. 3a, which shows the time course of the transmembrane voltage u , the Fenton–Karma variable v (which accounts for inactivation of the fast inward current I_{fi}), and the currents I_{fi} and I_s at a point where the wave block occurs (marked by the filled square in Fig. 3b). The horizontal pink lines in Fig. 3a Upper and c show the voltage above which I_{fi} is inactivated by the v gating variable ($u = 0.15$). Because I_{fi} is responsible for excitation and thus wave propagation, inactivation of I_{fi} results in wave block.

Now let us explain the onset of new wave breaks. During spiral wave rotation (Fig. 3a Upper and c Inset), we see that the minimal diastolic value of the transmembrane potential initially is slightly below the pink (inactivation) line, resulting in recovery of the variable v up to values of ≈ 0.6 (Fig. 3a Lower), which allows recovery of I_{fi} required for generation of a new action potential. However, we also observed that the minimal diastolic voltage increased, and after the third action potential the transmembrane potential did not decrease below the inactivation value. As a result, the inactivation variable v was not recovered and remained at zero, and thus I_{fi} did not recover as well (around the vertical dashed line in Fig. 3a Lower). In the absence of the fast inward current, excitation is not possible, and wave propagation was blocked. This nonrecovery of the transmembrane

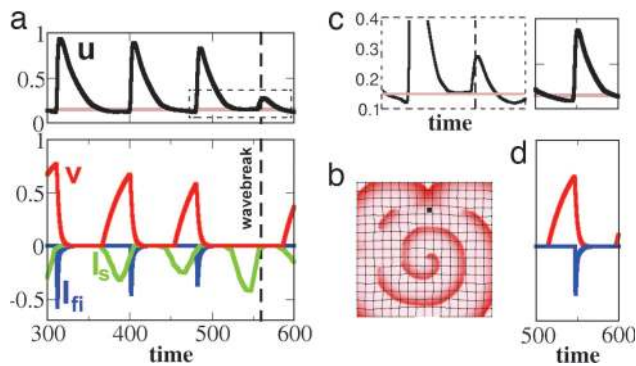


Fig. 3. Mechanism of breakup caused by mechanical activity. (a) Time courses of voltage u (black trace in *Upper*), stretch-activated current I_s multiplied by 100 (green trace in *Lower*), the fast inward current I_{fi} (blue trace in *Lower*), and the variable v (red trace in *Lower*), which are responsible for the inactivation of I_{fi} at the point marked by the filled square in *b*. The dashed line is located at 560 [t.u.], and the pink line is at $u = 0.15$. (b) Fragmentation of the spiral wave, showing the same simulation as in Fig. 1*b* but at time 560 [t.u.]. All parameters and conditions are the same as in Fig. 1*b*. (c) Magnification of the dashed rectangular region from *a*. (d) A similar computation as in *a* but in the absence of I_s ($G_s = 0$ in Eq. 8).

potential was caused by the stretch-activated current. We can see that I_s was maximal during the late repolarization phase, which prevented the voltage from decreasing below the pink line. To confirm this effect, we performed a similar simulation but with I_s blocked (Fig. 3*d*). In this case, repolarization continued below the inactivation threshold. Thus, the I_{fi} current was not inactivated, and the spiral wave did not break up.

The breakup we observed was caused by sodium current inactivation. However, although the representation of the sodium current in the Fenton–Karma model provides a qualitatively correct description of the activation–inactivation properties of this current, it is not based on experimental data of these processes. To underline the importance of the activation–inactivation processes for our mechanisms, we developed a modification of the Fenton–Karma model, which included biophysically based activation and inactivation curves of the fast sodium current. We replaced the Heaviside-based activation function $\Theta(u - 0.25)(u - 0.25)$ from Eq. 1 with the activation curve (m^3) from the TNNP model (24), scaled to the interval $[0, 1]$ (Fig. 2*a*) and the Heaviside inactivation function $\Theta(u_c - u)$ from Eq. 2 with the voltage-dependent inactivation curve $h \times j$ (Fig. 2*a*). Thus, in this modified model, activation and inactivation processes are based on experimentally measured properties of the sodium current. We studied spiral wave rotation with this model and found that with these modifications we also obtained mechanically induced breakup of the spiral wave. As in the case of the Fenton–Karma model, after a few rotations the spiral wave broke down into a complex spatiotemporal pattern (Fig. 2*b*). Overall, the breakup process was similar to that observed in the Fenton–Karma model; however, our modification of I_{fi} resulted in some increase in the wavelength of the spiral waves.

Spiral Wave Drift. We studied the dynamics of spiral wave rotation by using parameter values for which spiral breakup was absent in the absence of deformation. Under these conditions, the spiral wave rotation was stationary with a circular motion of the spiral tip (Fig. 1*a*). Using the same parameter values in the presence of mechanical activity, we observed drift of the spiral wave to the center of the medium (Fig. 4*a*) and subsequent meander of the spiral around the center. The meander pattern in Fig. 4*a* was a combination of two motions: a counterclockwise rotation of the spiral wave tip along a circular trajectory (similar to that in Fig. 1*a*), with the motion of the center of rotation of this circle after

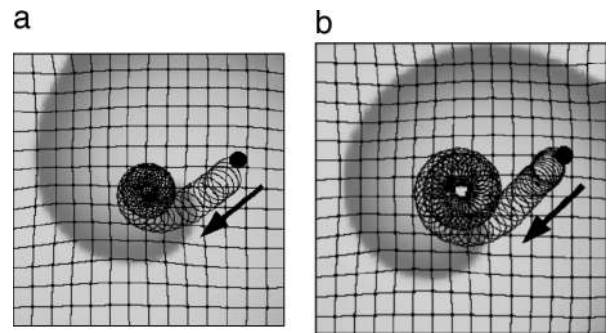


Fig. 4. Spiral wave drift caused by mechanical activity. (a) Initial position of a spiral wave tip (black circle) and the final state of the spiral wave after 120 rotations (shaded image) in a medium containing 141×141 grid points with 11×11 points per mechanics element and $G_s = 0.01$. The arrow indicates the direction of spiral wave drift, and the solid curve illustrates the trajectory of the spiral tip. (b) A similar simulation to that in *a* but in a medium containing 151×151 grid points. Other parameter values were the same as those for Fig. 1*b*, except $u_c = 0.25$, $\tau_1 = 95$, and $\tau_3 = 300$.

another circular trajectory in the clockwise direction. This tip trajectory was reproduced accurately in the complex plane $Z = X + iY$ (up to initial phases) by using:

$$Z(t) = R_0 \exp(i2\pi f_0 t) + R_1 \exp(-i2\pi f_1 t). \quad [9]$$

Eq. 9 describes a cycloidal motion that is a superposition of a clockwise spiral wave rotation with frequency f_0 along a circle of radius R_0 and a counterclockwise circular motion along the radius R_1 with frequency f_1 . For Fig. 4*a*, these parameters are $R_0 = 7.50$ [s.u.], $f_0 = 11.95 \times 10^{-3}$ [t.u.] $^{-1}$, $R_1 = 4.86$ [s.u.], $f_1 = 0.56 \times 10^{-3}$ [t.u.] $^{-1}$. We performed several simulations with different initial spiral wave locations, and in all cases, the spiral wave approached the center of the medium and meandered along a similar trajectory to that in Fig. 4.

We also have studied how the size of the medium affects spiral wave drift. Fig. 4*b* illustrates the behavior of a spiral wave in a larger medium (151×151 grid points, compared with the 141×141 grid in Fig. 4*b*). In this case, the spiral wave also drifted to the center, but its meander pattern was of larger overall dimension. This meander also was reproduced by using Eq. 9 with $R_0 = 7.50$ [s.u.], $f_0 = 11.95 \times 10^{-3}$ [t.u.] $^{-1}$, $R_1 = 10.67$ [s.u.], $f_1 = 0.37 \times 10^{-3}$ [t.u.] $^{-1}$. Thus, the change in medium size did not affect the spiral wave rotation (R_0 and f_0 are the same for Fig. 4*a* and *b*); however, the radius and the period of the circular meander trajectory were greater for the larger medium.

Fig. 5*a* shows the effect of medium size on the characteristics of the meander pattern. We observed that R_0 and f_0 remained constant, whereas R_1 increased and f_1 decreased with the increase in medium size. As a result, the radius of the meander pattern increased, and the speed along the circular trajectory $2\pi \times R_1 \times f_1$ increased only slightly with size (data not shown).

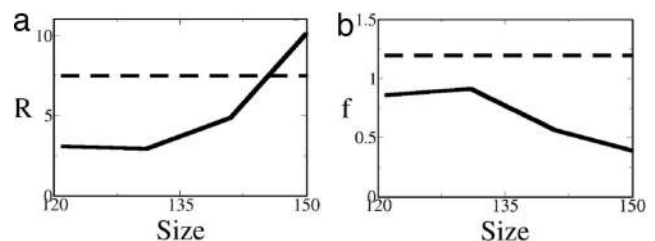


Fig. 5. Characteristics of meander patterns. (a) R_0 and R_1 in [s.u.] versus medium size (in grid points). (b) f_0 and f_1 in [t.u.] $^{-1}$ versus medium size.

In a similar manner to the spiral breakup analysis, we studied how this drift was modulated by the two feedback effects of deformation: the stretch-activated current I_s and the effect of tissue deformation of wave propagation. We observed that drift of the spiral wave occurred in the absence of I_s , although the meander pattern was not cycloidal (SI Fig. 8a). However, the drift speed was much slower than that in Fig. 4a. After 120 rotations, the spiral wave had drifted approximately one-third of the medium width, whereas by the same time in Fig. 4b, the spiral had approached and made several rotations about the center of the medium. In SI Fig. 8b, we see that I_s alone induced drift and meander of the spiral wave similar to that in Fig. 4a. The characteristics of the meander trajectories also were similar ($R_0 = 7.36$ [s.u.], $f_0 = 12.07 \times 10^{-3}$ [t.u.]⁻¹, $R_1 = 4.23$ [s.u.], $f_1 = 0.56 \times 10^{-3}$ [t.u.]⁻¹), although there was a small increase in the spiral wave frequency f_0 and a slight decrease in the radius of the circular motion R_1 compared with that of Fig. 4a. Thus, for these parameters, we conclude that the dominant factor driving spiral drift is the stretch-activated current.

We believe that the mechanism of this drift is similar to the resonant drift of spiral waves reported in refs. 25 and 26. As demonstrated in ref. 26, a periodical variation of the properties of an excitable medium in synchrony with the period of a spiral wave resulted in drift and subsequent stable meandering of the spiral wave tip. In our model, deformation of the medium also produced a periodical modulation of the tissue properties in synchrony with the spiral wave period as a result of the excitation–contraction coupling. Thus, the effects of mechanics in the present study are likely to be similar to the effects of periodical forcing during resonant drift, leading to drift and meandering attractors for spiral wave rotation.

Discussion

We have demonstrated that deformation has a pronounced effect on spiral wave rotation and can induce either breakup or drift and meander of spiral waves.

By using very general descriptions of the excitation–mechanics properties, our modeling has demonstrated that stretch-activated channels can induce spiral wave breakup. This conclu-

sion requires confirmation both experimentally and by using modeling studies involving detailed ionic descriptions of cardiac tissue. In support of the latter, we have shown that spiral breakup occurred as a result of inactivation of the fast inward current I_{fi} , which was caused by diastolic depolarization mediated by the stretch-activated current. Furthermore, the notion that the stretch-activated current can block action potential has been demonstrated by using the Beeler–Reuter ionic model for ventricular cells (20), for which it was shown that increasing the conductance of the stretch-activated current resulted in failure of excitation of cardiac cells (see figure 3 in ref. 20). Note also that inactivation of the fast sodium current by depolarization has been observed experimentally (e.g., ref. 23) and reproduced by using ionic models of cardiac tissue (27), for which it can cause block of propagation.

We suggest that the mechanism of spiral drift is similar to the resonant drift mechanism. Resonant drift of spiral waves in cardiac tissue has not been studied experimentally in biological tissues but has been shown to exist in detailed ionic models of cardiac tissue (28), as well as in experiments involving BZ reactions (26). Therefore, it is likely that these effects of mechanics on spiral wave dynamics also could be reproduced by using more detailed experimental and modeling studies in cardiac tissue and in BZ reaction.

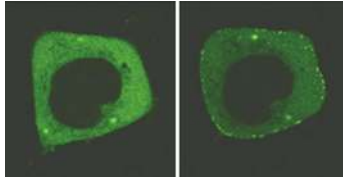
Here, we have presented a general study of spiral wave dynamics in a deforming medium, but many potentially important factors have been neglected, such as the fibrous anisotropy of cardiac tissue, which is important both for the electrical and mechanical properties of the heart. We chose not to consider this factor because the main aim of this study was to investigate the basic effects of mechanics on a general RD system. The influence of cardiac anisotropy is likely to add additional effects and will need to be addressed in future studies.

We thank Dr. F. Fenton, Prof. P. J. Hunter, and Dr. P. Kohl for valuable discussions. This research is funded by The Netherlands Organization for Scientific Research Grant 814.02.014. M.P.N. is supported by the Marsden Fund Council from New Zealand government funding, administered by the Royal Society of New Zealand.

1. Zaikin AN, Zhabotinsky AM (1970) *Nature* 225:535–537.
2. Winfree AT, Strogatz SH (1984) *Nature* 311:611–615.
3. Imbihl R, Ertl G (1995) *Chem Rev* 95:697–733.
4. Weijer C (2004) *Curr Opin Genet Dev* 14:392–398.
5. Lechleiter J, Girard S, Peralta E, Clapham, D (1991) *Science* 252:123–126.
6. Davidenko JM, Pertsov AM, Salomonsz R, Baxter W, Jalife J (1991) *Nature* 355:349–351.
7. Yoshida R, Takahashi T, Yamaguchi T, Ichijo H (1996) *J Am Chem Soc* 118:5134–5135.
8. Kohl P, Ravens U (2003) *Prog Biophys Mol Biol* 82:1–266.
9. McCulloch AD, Smaill BH, Hunter PJ (1987) *Am J Physiol* 252:H233–H241.
10. DiFrancesco D, Noble D (1985) *Philos Trans R Soc B* 307:353–398.
11. Kohl P, Hunter PJ, Noble D (1999) *Prog Biophys Mol Biol* 71:91–138.
12. Nash MP, Panfilov AV (2004) *Prog Biophys Mol Biol* 85:501–522.
13. Gray RA, Jalife J, Panfilov A, Baxter WT, Cabo C, Pertsov AM (1995) *Circulation* 91:2454–2469.
14. Garfinkel A, Qu Z (1999) in *Nonlinear Dynamics of Excitation and Propagation in Cardiac Tissue*, eds Zipes DP, Jalife J (Saunders, Philadelphia), pp 315–320.
15. Fenton F, Karma A (1998) *Chaos* 8:20–47.
16. Panfilov AV, Keldermann RH, Nash MP (2005) *Phys Rev Lett* 95:258104.
17. Hunter PJ, Nash MP, Sands GB (1997) in *Computational Electromechanics of the Heart*, eds Panfilov AV, Holden AV (Wiley, Chichester, UK), pp 345–407.
18. Hu H, Sachs F (1997) *J Mol Cell Cardiol* 29:1511–1523.
19. Zhang Y, Youm J, Sung H, Lee S, Ryu S, Ho W, Earm Y (2000) *J Physiol (London)* 523:607–619.
20. Vetter F, McCulloch A (2001) *Ann Biomed Eng* 29:414–426.
21. Trayanova N, Li W, Eason J, Kohl P (2004) *Heart Rhythm* 1:67–77.
22. Hill AV (1936) *Proc R Soc London* 119:305–355.
23. Hodgkin AL, Huxley AF (1952) *J Physiol (London)* 117:500–544.
24. ten Tusscher, KHWJ, Noble D, Noble PJ, Panfilov AV (2004) *Am J Physiol* 286:H1573–H1589.
25. Agladze KI, Davydov VA, Mikhailov AS (1987) *JETP Lett* 45:767–769.
26. Grill S, Zykov VS, Müller SC (1995) *Phys Rev Lett* 75:3368–3371.
27. Biktashev VN (2002) *Phys Rev Lett* 89:168102.
28. Biktashev VN, Holden AV (1995) *Proc R Soc London B* 260:211–217.

Corrections

IN THIS ISSUE, MEDICAL SCIENCES. For the “In This Issue” summary entitled “Carvedilol sidesteps G proteins,” appearing in issue 42, October 16, 2007, of *Proc Natl Acad Sci USA* (104:16392), the figure caption appeared incorrectly. The online version has been corrected. The figure and its corrected caption appear below.



Carvedilol recruits β -arrestin to the β 2-adrenergic receptor. The β -arrestin2-GFP is shown in green.

www.pnas.org/cgi/doi/10.1073/pnas.0710562104

PERSPECTIVE. For the article “Powering the planet: Chemical challenges in solar energy utilization,” by Nathan S. Lewis and Daniel G. Nocera, which appeared in issue 43, October 24, 2006, of *Proc Natl Acad Sci USA* (103:15729–15735; first published October 16, 2006; 10.1073/pnas.0603395103), the authors note that in Fig. 1, the charges shown in the solar fuel cell are on the wrong sides of the cell. The holes should be at the anode, and the electrons should be at the cathode. This error does not affect the conclusions of the article. The corrected figure and its legend appear below.

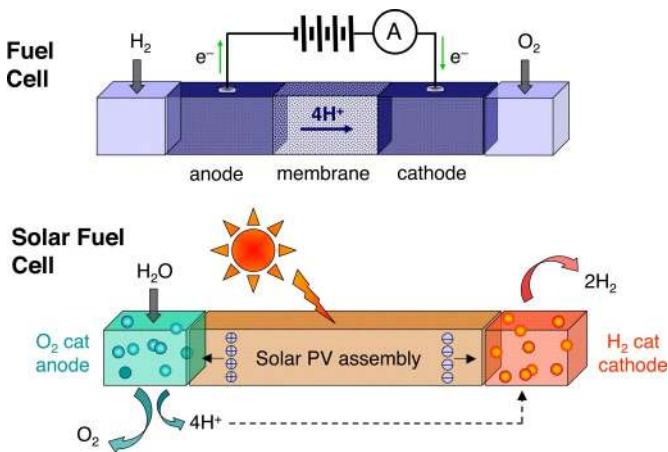


Fig. 1. H_2 and O_2 are combined in a fuel cell to generate a flow of electrons and protons across a membrane, producing electrical energy. The solar fuel cell uses light to run the electron and proton flow in reverse. Coupling the electrons and protons to catalysts breaks the bonds of water and makes the bonds H_2 and O_2 to effect solar fuel production.

www.pnas.org/cgi/doi/10.1073/pnas.0710683104

BIOPHYSICS. For the article “Drift and breakup of spiral waves in reaction–diffusion–mechanics systems,” by A. V. Panfilov, R. H. Keldermann, and M. P. Nash, which appeared in issue 19, May 8, 2007, of *Proc Natl Acad Sci USA* (104:7922–7926; first published April 27, 2007; 10.1073/pnas.0701895104), the authors note that on page 7922, right column, the first sentence in *Mathematical Model*, “Our RDM model is based on a three-variable Fenton–Karma RD model for cardiac excitation (15), coupled with the soft-tissue mechanics equations described in refs. 12 and 16 . . . , where $\Theta(x)$ is the standard Heaviside step function: $\Theta(x) = 1$ for $x \geq 0$ and $\Theta(x) = 0$ for $x < 0$,” should instead read: “Our RDM model consists of RD equations developed by F. H. Fenton (personal communication) and is based on a three-variable Fenton–Karma RD model for cardiac excitation (15), coupled with the soft-tissue mechanics equations described in refs. 12 and 16 . . . , where $\Theta(x)$ is the standard Heaviside step function: $\Theta(x) = 1$ for $x \geq 0$ and $\Theta(x) = 0$ for $x < 0$.” Additionally, on page 7923, left column, beginning on line 10 of the text, the formula for I_{si} is incorrect in part. The portion of the formula appearing as “ $(0.46 + 0.085 \cdot \tanh[k(u - 0.5)])$ ” should instead appear as: “ $(0.23 + 0.085 \tanh[10(u - 0.65)])$.” Thus, the corrected formula should read $I_{si}(u, w) = \Theta(u - 0.2)uw(0.23 + 0.085 \tanh[10(u - 0.65)])$. Finally, on page 7926, in the first sentence of the Acknowledgments, the authors would like to more specifically acknowledge the assistance of Dr. Fenton. Therefore, “We thank Dr. F. Fenton, Prof. P. J. Hunter, and Dr. P. Kohl for valuable discussions” should instead read: “We are grateful to Dr. F. H. Fenton, who kindly provided equations used in the construction of our RDM model, and to Prof. P. J. Hunter and Dr. P. Kohl for valuable discussions.” These errors do not affect the conclusions of the article.

www.pnas.org/cgi/doi/10.1073/pnas.0710559104